Physical properties of MgO at deep planetary conditions

R. Musella, S. Mazevet, F. Guyot

Physical properties of MgO at deep planetary conditions

R. Musella,[1] S. Mazevet,[1,2] and F. Guyot[3]

[1]*LUTH, Observatoire de Paris, Paris Sciences et Lettres (PSL) University, CNRS, Université Paris Diderot, 92195 Meudon Cedex, France*

[2]*CEA-DAM-DIF,91280 Bruyeres le Châtel, France*

[3]*Institut de Minéralogie de physique des Matériaux et de Cosmochimie (IMPMC), Museum National d'Histoire Naturelle, Sorbonne Université, IRD, CNRS, 75005 Paris, France*

(Received 31 May 2018; revised manuscript received 8 October 2018; published 25 February 2019)

Using *ab initio* molecular dynamics simulations, we calculate the physical properties of MgO at conditions extending from the ones encountered in the Earth mantle up to the ones anticipated in giant planet interiors such as Jupiter. We pay particular attention to the high-pressure melting temperature throughout this large density range as this is a key ingredient for building accurate planetary interior models with a realistic description of their inner cores. We compare our simulation results with previous *ab initio* calculations that have been so far limited to the pressure range corresponding to the Earth mantle and the B1-B2 transition around 6 Mbar. We provide our results for both the equation of state and high-pressure melting curve in parametric forms for direct use in planetary models. Finally, we compare our predictions of the high-pressure melting temperature with various planetary interior profiles to deduce the state of differentiated layer within the core made of MgO in differentiated cores of various types of planets and exoplanets.

DOI: 10.1103/PhysRevB.99.064110

I. INTRODUCTION

As a major constituent of the Earth mantle, the physical properties of magnesium oxide up to about 1 Mbar (1 Mbar = 100 GPa) have been the subject of extensive studies on both the experimental and theoretical sides [1]. For decades, this was especially the case for the equation of state (EOS) and the high-pressure melting temperature that are key ingredients to model the (Mg,Fe)O ferropericlase component in the Earth and put constraints on the solid or liquid nature of the lower mantle [2]. In this pressure range relevant to the physics of the Earth mantle, MgO is found to be remarkably stable in the B1 (NaCl) structure (periclase) with some discrepancies noted between the calculated and measured melting temperature [3].

With the continuous discovery of terrestrial exoplanets several times the size of the Earth, there is now a pressing need to extend our knowledge of the phase diagram of a few key planetary constituents up to several Mbar and well beyond conditions encountered in the Earth mantle [1]. In particular, the modeling of super-Earths, whose density is similar to that of the Earth but with mass up to 10 times the one of the Earth requires, for example, to extend our knowledge of the phase diagram of MgO up to 15 Mbar [4–6]. This jump by an order of magnitude of the pressure range that needs to be described is a significant challenge for both experiments and theoretical methods.

In addition to the large amount of experimental data and theoretical work reported for periclase at mantle conditions [1], laser-shock compression has been recently used to constrain the MgO phase diagram well beyond Earth mantle conditions. A first set of experiments identified discontinuities in the shock velocity data as a transformation from the B1 (NaCl) to the B2 (CsCl) structure at 4.5 M bar and 5000 and 7000 K and melting at 6 Mbar and about 12 000 K [7] using reflectivity measurements and assuming metallization upon melting. This B1-B2 transition was previously predicted by density functional theory (DFT) calculations and corresponds to an increase in coordination number of the Mg atoms from 6 to 8 atoms of oxygen [2]. These indirect constraints on the high-pressure phase diagram were followed up by high-power laser experiments that identified the B1-B2 transition directly using diffraction measurements and ramp loading to remain well below the temperature reached upon direct shock while reaching similar pressures [8]. These series of experimental measurements provide a first sketch of the high-pressure phase diagram of MgO with a B1-B2 transition occurring between 4 and 6 Mbar with a negative Clapeyron slope, a B2 structure stable up to 9 Mbar, and melting anticipated to occur at around 12 000 K at 6 Mbar. This pioneer work has triggered intense experimental and theoretical activities for the past few years and there are currently heated debates regarding the exact pressure-temperature location of these phase transitions up to below 7 Mbar [9–13].

In this paper, we use DFT simulations to significantly extend the phase diagram of MgO to encompass the conditions anticipated not only in super-Earths of up to 10 Earth mass (15 Mbar), but also to the ones expected in the cores of icy giant and giant planets (100 Mbar). MgO is indeed one end-member component in the core of these massive planets and could even be directly present as one dissociation product of the stable silicates $MgSiO_3$ or Mg_2SiO_4 that constitute planetary embryos in the core accretion model [14]. We paid particular attention to the high-pressure melting curve calculated across this up to now unexplored pressure range as this is required for the modeling of giant planets by providing an additional constraint on the nature of their inner cores. We also revisit the pressure region around 5 Mbar and compare our results for the B1-B2 transition and high-pressure melting

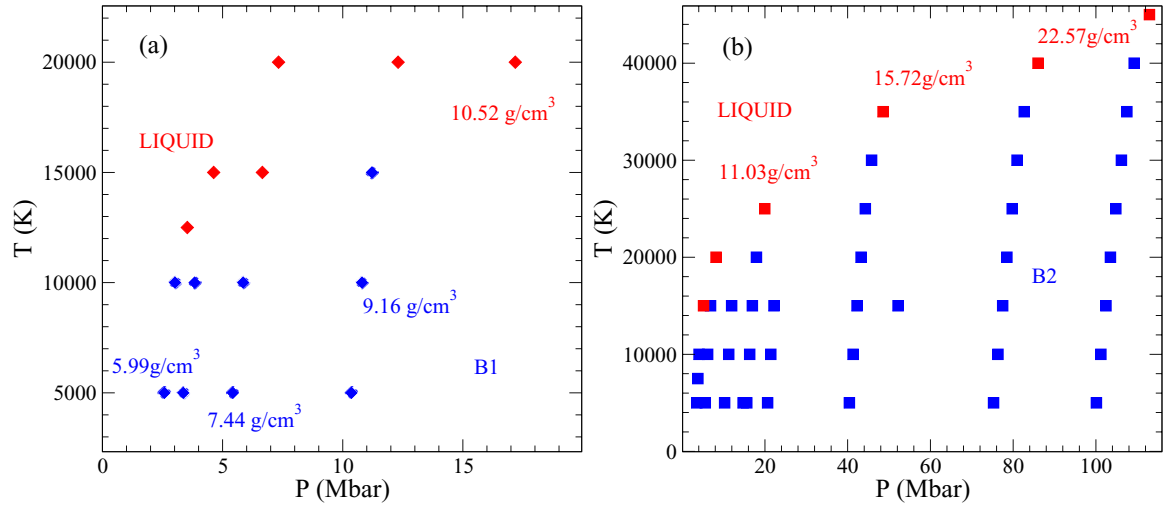

FIG. 1. (a) EOS points obtained with simulations initially started in the B1 phase. (b) EOS points obtained with simulations initially started in the B2 phase.

temperature with the large amount of theoretical and experimental work previously reported on.

II. *AB INITIO* SIMULATION RESULTS

A. Computational details

We carried out the *ab initio* molecular dynamics simulations using the ABINIT [15] electronic structure package. This consists in treating the electrons quantum mechanically using finite-temperature density functional theory (DFT) while propagating the ions classically on the resulting Born-Oppenheimer surface by solving the Newton equations. We used the local density approximation (LDA) with the Ceperley-Alder parametrization of the exchange correlation functional [16] that provides an equilibrium volume of 73.33 $Å^3$, closer to the experimental measurement 74.7 $Å^3$, than in the generalized gradient approximation (GGA) for MgO [17]. While this somewhat arbitrary choice does not guarantee a better behavior of the LDA formulation against the GGA one at high pressures, we point that sample calculations performed in the tens of Mbars range indicate that the difference between the two tends to become less significant in the extreme pressure range investigated here.

We used two sets of projected augmented wave (PAW) pseudopotentials to cover the entire density range considered here, from 6 to 22.5 g/cm^3. For densities up to 9 g/cm^3, we used two projected augmented wave (PAW) pseudopotentials generated by Jollet *et al.* [18]. These pseudopotentials are designed to reproduce accurately the all-electron LAPW results obtained for the individual atomic species. This warrants that no spurious effects due to the pseudization procedure are at play. For the two atomic species considered here, these pseudopotentials consist in a PAW cutoff radius of, respectively, $1.7a_B$ and $1.2a_B$. For both pseudopotentials, the $1s^2$ state only is kept as a core state while the remaining electrons are treated as valence orbitals. To reach densities above 9 g/cm^3 while ensuring that the overlap of the PAW spheres remains marginal, we use the ATOMPAW [19] package to generate pseudopotentials with significantly smaller cutoff radius. For this second set of pseudopotentials, the cutoff radii were fixed at $r_{paw} = 1.1a_B$ and $r_{paw} = 1.0a_B$ for, respectively, the magnesium and oxygen atomic species. The accuracy of the two sets of pseudopotentials produced was inferred by comparing the $T = 0$ K EOS (cold curve) obtained for the B1 phase with the all-electron LAPW results [17]. The static calculations were performed using the B1 unit cell with a 8^3 **k**-points grid and a plane-wave cutoff of 28 and 36 Ha for, respectively, the soft and harder sets of pseudopotentials.

The molecular dynamics runs were performed using the finite-temperature formulation of DFT as laid out by Mermin [20] while the equations of motion for the ions were integrated using the isokinetics ensemble. For each simulation runs, this consists in keeping the number of particles as well as the volume of the simulation cell fixed while rescaling the atom velocities at each time step to keep the temperature constant. While it is well documented that this ensemble is not formally corresponding to the canonical ensemble, it is used here in a situation where the properties calculated such as the EOS or the melting temperature are not sensitive to the use of a more refined thermostat [21]. We typically used a time step of 1 fs at all thermodynamics conditions. For the EOS calculations, we performed the simulations at the Γ point and using 128 atoms in the simulation cell. We ensured that the results obtained for the pressure, internal energy, and ionic structure are converged to better than 1% for both the B1 and B2 phases by doubling the number of atoms and considering 256 atoms at a few sample P-T conditions. Additional details on the simulation parameters can be found in [22].

B. Equations of state

Figures 1(a) and 1(b) show the EOS points obtained for simulations initially started in, respectively, the B1 and B2 phases. For the B1 phase, we calculate EOS points using 128 atoms along six different isochores, 5.99 g/cm^3, 6.45 g/cm^3, 7.44 g/cm^3, 9.16 g/cm^3, 10.52 g/cm^3, and 11.54 g/cm^3, and for temperatures ranging from 5000 to 20 000 K. For the first

four isotherms, we find results consistent with previous works and the latest work of Cebulla *et al.* who explored extensively this portion of the phase diagram below 10 Mbar. We note that inspection of the correlation functions indicates that the B1 phase is unstable on the two highest isochores.

Figure 1(b) shows the EOS points obtained when starting the simulation in the B2 structure. To reach pressures relevant to the interior of giant planets, we performed simulations along eight different isochores, 6.76 g/cm^3, 7.79 g/cm^3, 9.64 g/cm^3, 11.03 g/cm^3, 12.20 g/cm^3, 15.72g/cm^3, 20.10 g/cm^3, and 22.57 g/cm^3, with temperatures varying from 5000 to 45 000 K. In contrast to the B1 structure that rapidly becomes unstable past the B1-B2 transition, inspection of the correlation functions indicates that the B2 structure remains stable up to 120 Mbar. While this does not formally warrant that the B2 structure is the lowest-energy phase up to these extreme densities, the stability found combined with the high coordination number of Mg by oxygen in the B2 phase is an indication that no other phase is expected beyond the B1-B2 transition.

In Figs. 1(a) and 1(b), we also display the state of the system at each pressure-temperature point by using the average mean-square displacement. The average mean-square displacement is calculated using the two atomic species. We point out that close inspection of the mean-square displacement for the individual atomic species close to melting suggests that both participate in melting with no indication of partial melting on sublattices. Inspection of Figs. 1(a) and 1(b) shows that the melting temperature rises rapidly to reach 40 000 K for pressures beyond 100 Mbar. It also shows that each phase exhibits a distinct pressure dependence of its melting temperature. It is well documented [23] that this basic approach leads to an overestimation of the melting temperature due to the limited number of atoms that can be used in *ab initio* simulations. We will turn below to the numerically intensive two-phase simulation method to reach a more precise calculation of the melting temperature up to the conditions encountered in giant planet interiors and use this first estimation of melting as a boundary to develop a simple parametrization of the *ab initio* results.

For a convenient use of our *ab initio* results in planetary modeling, we further adjusted a parametrization of the Helmotz free energy $F(V,T)$ to the *ab initio* results. As developed further in Bouchet *et al.* [23], this consists in expressing the Helmoltz free energy $F(V,T)$ of the solid in the adiabatic approximation as

$$F = E_{\rm cold}(V) + F_{\rm harm}(V,T) + F_{anh}(V,T) + F_{el}(V,T), \quad (1)$$

where $E_{\rm cold}$ is the cold curve and represents the potential part of the free energy at zero temperature. $F_{\rm harm}(V,T)$ is the harmonic phonon contribution that can be obtained using linear response theory and the quasiharmonic approximation for the ion motions, $F_{anh}(V,T)$ represents the correction due to anharmonic effects, and $F_{el}(V,T)$ represents the electronic contribution.

For the cold curve contribution, we use the Holzapfel form [24] as it provides the correct Thomas-Fermi limit at infinite compression [3]. As such, it is formally more appropriate than other parametrizations such as the Vinet or Birch-Murnaghan functional forms to cover the compression range considered here. Within this parametrization, the pressure is given as

$$P(V)_{\rm cold} = 3K_0X^5(1-X)\exp[c_0(1-X)][1+c_2X(1-X)] \quad (2)$$

with $X=(V/V_0)$, $c_0=-\ln(3K_0/P_{FG0})$, $P_{FG0}=1003.6\,(Z/V_0)^{(5/3)}$, and $c_2=3/2(K'-3)-c_0$. V_0 is the equilibrium molar volume in cm^3/mole while P_{FG0} is given in GPa.

TABLE I. Set of parameters obtained by our fitting procedure of the B2 phase.

V_0 (cm^3/mole)	K_0 (GPa)	K_0' (GPa)	Θ_0 (K)	γ_0
10.970	120.76	4.803	447.906	1.755
β	γ_∞	a_0 (K^{-1})	m	
−0.530	-7.579×10^{-2}	-1.341×10^{-4}	0.660	

The thermal contribution is parametrized using the Einstein model where

$$P_{\rm harm} = \gamma E_{\rm harm}/V \quad (3)$$

with $E_{\rm harm}=3nR[\Theta/2+\frac{\Theta}{\exp(\Theta/T)-1}]$, R is the gas constant, and n the number of atoms, equal to two in the present case. The Gruneisen parameter is given by

$$\gamma = \gamma_\infty + (\gamma_0-\gamma_\infty)(V/V_0)^\beta, \quad (4)$$

where γ_0 and γ_∞ represent its values at, respectively, ambient conditions and infinite compression following Al'tshuler *et al.* [25]. The Einstein temperature Θ is expressed as

$$\Theta = \Theta_0(V/V_0)^{-\gamma_\infty}\exp\left[\frac{\gamma_0-\gamma_\infty}{\beta}[1-(V/V_0)^\beta]\right]. \quad (5)$$

In these relations, Θ_0, γ_∞, γ_0, and β are fitting parameters that formally do not carry any physical meaning. Finally, as the anharmonic and electronic terms have the same temperature dependence [26], we used a single functional form given by

$$P_{ae} = \frac{3R}{2V}ma_0x^mT^2, \quad (6)$$

to represent both contributions with a_0 and m two fitting parameters.

As for the case of iron [23], we fitted globally the *ab initio* results using the complete functional form and without separating the cold $E_{\rm cold}(V)$ contribution from the thermal one. This leads to the nine parameters given in Table I. This allows to reproduce the *ab initio* pressure to an accuracy of better than 2%. We note that we started the fit in the B2 phase slightly below the B1-B2 transition and for a density $\rho=6.51$ g/cm^3.

C. High-pressure melting

We used the computationally intensive two-phase method as described in Bouchet *et al.* [27] to evaluate the high-pressure melting temperature and correct for the overheating observed when considering direct bulk melting as used in the previous section. This simulation approach basically consists

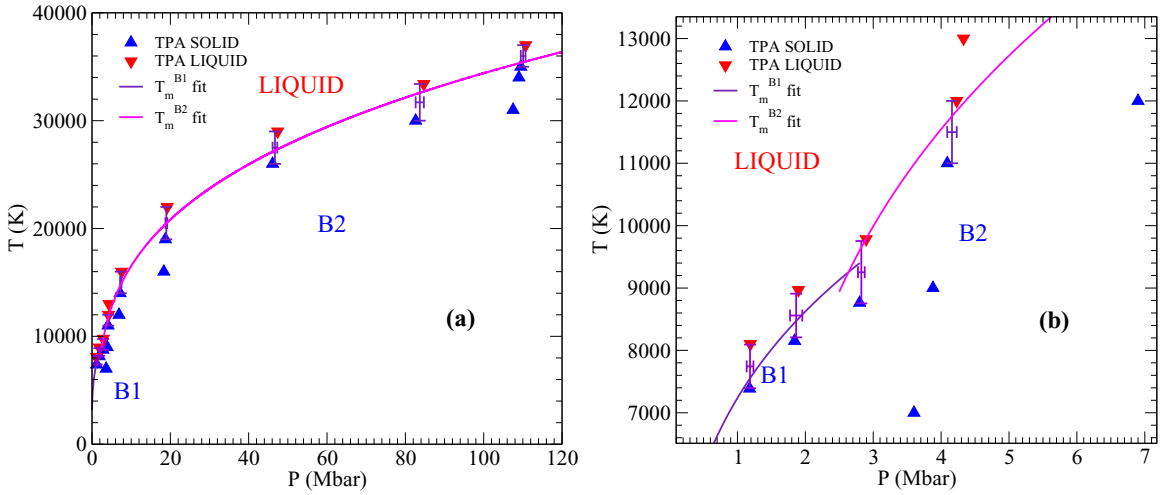

FIG. 2. (a) High-pressure melting temperature obtained with simulations initially started using the B1 and B2 phases. (b) Zoom at pressures below 10 Mbar. The color scheme indicates the final state after equilibration in the liquid (red) and in the solid (blue).

in using a supercell initially set up with both a liquid and a solid part brought in contact and equilibrated. Since the first implementations, the equilibration runs have been performed at constant volume [(N,V,T)/(N,V,E) ensembles] [28] or constant pressure [(N,p,T) ensemble] [29]. In both cases, the cell equilibrates toward either the solid or liquid state. This should be distinguished from the coexistence simulations [30], where the equilibration run is performed in the (N,V,E) ensemble with the temperature adjusting to the melting temperature while both phases are let to coexist.

In the results presented here, the initial conditions were created by considering the simulation results obtained in the EOS calculations and using 128 atoms. Namely, along a given isochore, we set up a 256-atom simulation cell. We used the liquid and solid structures previously obtained at the same density, at the lowest and highest temperatures where melting and solid were observed, and equilibrated them at the required temperature for a few hundred steps. While the final results are not that sensitive to such a careful setup of the initial conditions, it remains more efficient from a computational standpoint to start from partially equilibrated cells. Like Root *et al.* [10] at low pressures, we do not find at higher pressures the strong anisotropic stress reported by Belonoshko *et al.* [3] when using this initialization procedure.

The equilibration runs were performed in the (N,V,T) ensemble and the final state obtained carefully checked against the corresponding bulk simulations to ensure that no metastable state occurred. As the direct bulk melting results provide an upper bound for the melting temperature, the two-phase simulations were only performed along each isochore and for temperatures below the one obtained with bulk melting. Simulations are performed with decreasing temperature until melting is observed. All the simulations used 256 atoms and were performed at the Γ point. Previous studies [2] showed that this number of atoms is sufficient to obtain accurate high-pressure melting properties.

Figures 2(a) and 2(b) show the results obtained, respectively, over the whole pressure range and at conditions below 7 Mbar. As the melting temperature is bracketed using this method, we take, as melting temperature along an isochore, the midpoint between the lowest temperature where the simulation is showing melting and the highest where it equilibrates to a solid. We further associate to this melting temperature error bars that correspond to the average of these closest values. In effect, this corresponds to the uncertainty on the high-pressure melting temperatures calculated with this method as there are no warranties that the melting temperature fall exactly at the midpoint. Figure 2(a) shows a rapid increase of the melting temperature in the B2 phase that reaches 34 000 K for pressures above 100 Mbar. We also see that the direct bulk melting method used above overestimates melting significantly. At 100 Mbar, we find that the melting temperature predicted by the two-phase method is lower by 14%. We further note that the melting temperature in the B2 phase follows a simple Simon law with a slope of the melting temperature steadily decreasing as the pressure increases. Figure 2 shows a fit of the *ab initio* results using the Simon-Glatzel law for each of the two phases. This empirical law relates the melting temperature T_m to the pressure using the relation

$$T_M = T_{\text{ref}}\left(\frac{P_M - P_{\text{ref}}}{a} + 1\right)^{(1/c)}, \tag{7}$$

where T_{ref} and P_{ref} are the temperature and pressure of the triple point while a and c are two adjustable parameters. For the B1 phase, we completed the *ab initio* two-phase simulation results with the two lower density points of Alfe [2] and the experimental melting temperature at normal conditions to perform the fit. For the B2 phase, we iteratively adjusted the reference point, which corresponds in this case to the position of the triple point, to match the melting temperature of the

TABLE II. Coefficients of the Simon-Glatzel form fitting the *ab initio* results in the B1 and B2 phases.

Phase	T_{ref} (K)	P_{ref} (Mbar)	a (Mbar)	c
B1	3152	0	0.043	3.83436
B1	9255	2.6363	1.25668	3.32258

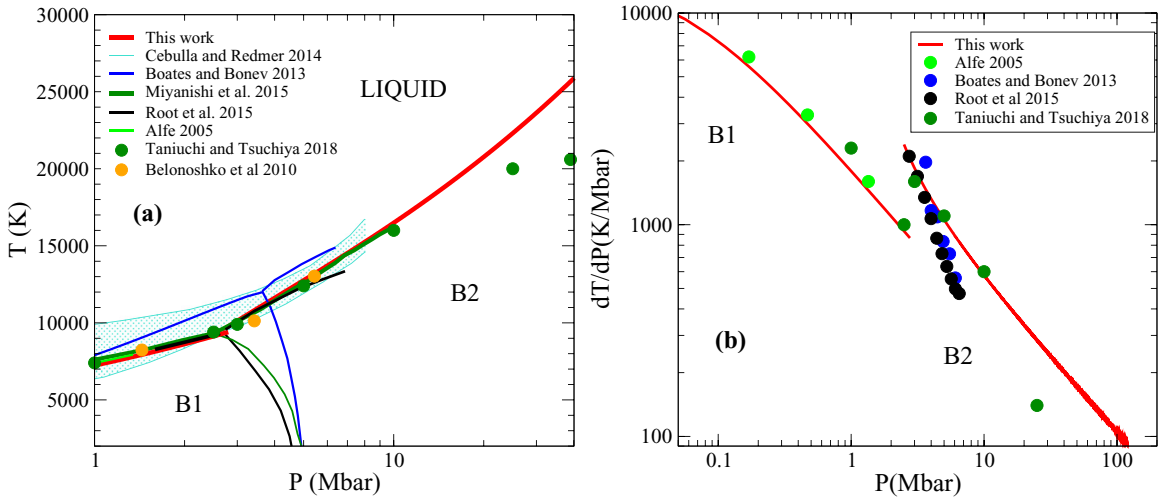

FIG. 3. (a) Comparison between the high-pressure melting curve obtained in this work and previous results. (b) Comparison between the slopes of the melting curve (dT/dP) obtained in this study with previous work.

B1 phase and provide at the same time an accurate evaluation of the melting temperature throughout the entire pressure range. Using this approach, we estimate the location of the triple point at ($P_{\rm ref} = 2.63$ Mbar; $T_{\rm ref} = 9250$ K). Table II shows the coefficients obtained for each phase. We now turn to comparing our results with previous estimations up to 10 Mbar.

III. COMPARISON WITH PREVIOUS WORK

We compare in Fig. 3 our estimation of the high-pressure melting curve for the B1 and B2 phases with the latest theoretical estimations. Following the pioneer work of Alfe [2], who made the first calculation of the high-pressure melting temperature up to the pressure encountered at the Earth core-mantle boundary using DFT based coexistence simulations, several predictions followed to extend this work beyond the B1-B2 transition. Figure 3(a) shows that in the B1 phase, our prediction agrees nicely with the estimation of Root *et al.* [10] and Miayanishi *et al.* [12] and contrasts with the one of Boates and Bonev [13]. This latter prediction, while based on *ab initio* calculations relies on a unconventional approach to estimate the ionic entropy in the liquid. Our calculation in the B1 phase confirms that the prediction of Boates and Bonev [13] is not correct beyond 1 Mbar due to the approximation used in their free-energy calculation. A closer inspection shows slight differences of a few hundred Kelvin between the three other calculations but they remain well within the error bar of the method. Figure 3 shows that the agreement is also satisfactory with the result of Belonoshoko *et al.* who used the Z method [31] to estimate the melting temperature in the B1 phase and around the B1-B2 transition [3]. This comparison for the melting temperature obtained in the B1 phase is intended to validate our simulation parameters to calculate the high-pressure melting in the B2 phase. It does not completely represent the large body of work performed both experimentally and theoretically below 5 Mbar. An up-to-date review can be found in Duffy *et al.* [1].

Figure 3(a) shows that the comparison in the B2 phase is more contrasted. While our prediction of melting in the B2 phase agrees with the prediction of Root *et al.* [10], Belonoshko *et al.* [3], and Miyanishi *et al.* [12] up to 5 Mbar, we see a departure with the former at 7 Mbar. The single point in the B2 phase obtained using the Z method by Belonoshko *et al.* [3] is in good agreement with our prediction at 7 Mbar. In contrast, we find a rather severe disagreement with the latest predictions of Taniuchi *et al.* [32]. The differences between the various predictions can be better highlighted by considering the slope of the melting curve dT/dP.

Figure 3(b) displays the slope of the melting curve as a function of pressure as obtained from the various predictions. We see, as expected, a satisfying agreement between the various predictions for the B1 phase, with a slope continuously decreasing as the pressure increases. In the B2 phase, we see that all the predictions agree reasonably above the B1-B2 transition occurring around 3 Mbar and up to 6 Mbar. In agreement with what we noticed previously for the melting curve above 6 Mbar, we see that the Root *et al.* [10] prediction for the slope of the melting curve departs from the prediction made in this work as well as with the prediction of Miyanishi *et al.* [12] at higher pressures. We find a good agreement with the result of Miyanishi *et al.* [12] up to the highest pressure they investigated, 10 Mbar.

However, the two additional points recently published at 25 and 39 Mbar [32] significantly depart from our predictions. This is especially the case for the point at the highest pressure, 39 Mbar, where we see a difference of up to 20%. We have no clear explanation for this difference and can only point out differences between the two calculations. Taniuchi *et al.* [32] used an innovative thermodynamic integration method that has not been calibrated on benchmark systems so far. They furthermore use Vanderbilt pseudopotentials that are less robust at the extreme pressure range considered here. This contrasts with the current work that uses PAW pseudopentials well calibrated to the extreme conditions encountered here and the overused two-phase approximation. Detailed comparisons are, however, needed for either the high-pressure behavior of the pseudopotentials or the simulation method to

identify clearly the source of this discrepancy.[1] The difference between the various results can be better highlighted by considering the slope of the melting curve $\frac{dT}{dP}$.

Figure 3(b) indicates that the slope is steadily decreasing as pressure increases. This is also the case in the calculations of Miyanishi *et al.* [12] up to 10 Mbar. As can be expected from Fig. 3(a), the extension of the calculations by Taniuchi *et al.* [32] indicates a sudden change of slope that we do not find in our calculation. Additional calculations at even higher pressures and extending up to 100 Mbar may help clarify the origin of the discrepancies and validate their two extreme points. Using our method, we find that the slope decreases steadily, by up to an order of magnitude from the B1-B2 transition at 3 Mbar up to the regime relevant to giant planet interiors. For Jupiter, the largest planet in our solar system, this regime occurs between 40 and 70 Mbar. By considering the Clausius-Clapeyron relation $dT/dP = v_m/s_m$, with v_m and s_m, respectively, the volume and entropy changes at melting. This continuous decrease of the slope suggests that the volume change and probably also the entropy at melting continuously decrease as pressure increases. This suggests that MgO follows the standard behavior of materials with a behavior in the B2 phase similar to what was pointed out for the B1 phase by Alfe [2].

We also stress that our estimation of the B2 high-pressure melting below 5 Mbar remains, within the error bar of the method, similar to the result of Root *et al.* [10]. Furthermore, our crude estimation of the triple point, based on fitting the high-pressure melting temperature in the B1 and B2 phases using a Simon-Glatzel law [33] is also consistent with their result. As such, we confirm their analysis regarding the position of the B1-B2 transition and the discrepancies with the experimental measurement of Coppari *et al.* [8] who found the solid-solid B1-B2 transition occurring at 6 Mbar for temperatures of 5000 K. Similarly, our results fail to interpret the discontinuity observed in the experimental measurements of McWilliams *et al.* and Bolis *et al.* who both used decaying shocks to probe the equation of state of MgO at pressures around 5 Mbar and temperatures close to 10 000 K. The discontinuity observed in the (P,T) space does not correspond to either the B1-B2 transition or the high-pressure melting temperature as calculated by *ab initio* simulations. As our results are similar to those of Root *et al.* [10], this complete comparison with the experimental data below 5 Mbar is thus not reproduced here. We point out, however, that the analysis of the density of states and the calculation of the electrical conductivity using the Kubo-Greenwood formulation [34] in each of the three phases unambiguously indicates that MgO is a semiconductor in the two solid phases and is metallic in the liquid phase [22].

IV. IMPLICATION FOR PLANETARY MODELING

We compare, in Fig. 4, our prediction for the B2 high-pressure melting temperature with planetary interior profiles

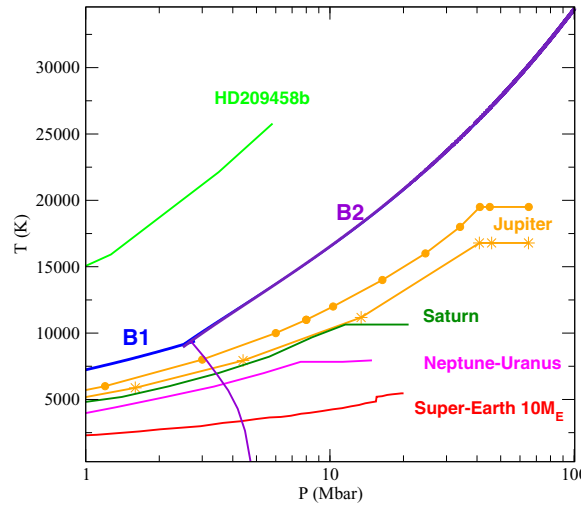

FIG. 4. Comparison between the B2 high-pressure melting temperature with planetary interior profiles.

representative of the various objects currently observed. These interior profiles are all obtained considering the planet as made of successive layers of varying composition in hydrostatic equilibrium [35]. For Jupiter and Saturn, this mainly consists in an envelope made of hydrogen and helium with a core represented as a mixture of water and silicates. For Neptune and Uranus, the paradigm consists in considering three layers, an H-He envelope, a large water mantle, and a central core made of silicates. Super-Earths are approximated as a silicate mantle, that can contain a significant amount of MgO, with an iron core. Within this picture, MgO is expected to be found either from the initial formation or as a dissociation product of $MgSiO_3$ or Mg_2SiO_4 [36]. Figure 4 shows various interior profiles for these three types of planets. For Jupiter, we show the two latest estimations [37] of Militzer *et al.* [38] and Nettelmann *et al.* [39]. The plateau above 40 Mbar represents the conditions encountered in the core where an isothermal approximation is used when solving the hydrostatic equations. We see in Fig. 4 that, if present, MgO would be found in a B2 solid phase. We indeed see that the conditions anticipated in the core by either models are well below the melting temperature predicted in this work. For pressures above 40 Mbar, we predict melting temperatures steadily increasing from 25 000 K. This is also the case for the other giant planet of our solar system, Saturn, where the conditions at the core are predicted to be above 10 Mbar and temperature around 11 000 K [35]. The melting temperature of the B2 phase is predicted to be close to 50% higher and thus well above the core conditions.

As we turn to the two icy giants, Neptune and Uranus, less extreme conditions prevail in the core [35]. The pressure is estimated to be on the order of 7 Mbar and higher and the temperature around 7500 K. The estimated temperature for the core is now a factor of 2 lower than the predictions of the high-pressure melting temperature made in this work and corroborated by two other *ab initio* calculations as described in the previous sections. For the last type of planets, super-Earths, we show in Fig. 4 a profile for a planet of $10M_E$ (M_E Earth mass) [4,6,40]. The conditions encountered in

[1]Further details on the pseudopotentials, such as the 0-K EOS (cold curve), can be found in [22].

the silicate mantle are estimated to be below 5000 K up to 15 Mbar. There also, the MgO melting curve is at higher temperatures than the planetary profile In Fig. 4, the discontinuity at 15 Mbar represents the interface between the envelope (or mantle) and the core.

Figure 4 shows that the only system where MgO could be anticipated in a liquid state in the planet interior is a hot exoplanet such as HD209458b. In the centers of giant and icy giant planets of the solar system, our calculations show that MgO is in a solid B2 state if present. This is also the case for super-Earths up to $10M_E$. We also point out that the result obtained in this work for the high-pressure temperature of the B2 phase also allows us to anticipate that this is likely the case for giant exoplanets several times the size of Jupiter. Indeed, interior structure calculations for a planet three times the size of Jupiter and of comparable age indicate that the core spans pressures from 300 to 400 Mbar and temperatures around 40 000 K. As we found by direct calculations that the melting temperature reached comparable value by 100 Mbar with a positive slope, we anticipate that MgO will be in the B2 solid phase in these objects.

V. SUMMARY

We calculated the EOS and high-pressure melting curve of MgO in the B1 and B2 phases up to 120 Mbar. Exhaustive comparison with previous work shows satisfying agreement with previous estimations for both the EOS and the high-pressure melting temperature in both phases and up to 10 Mbar. Beyond this pressure, we point out an unresolved discrepancy with the two high-pressure extension points calculated by Taniuchi *et al.* [32]. We provide both the EOS and melting curve in parametric form for a direct use in planetary modeling. Direct comparison with various estimations of the interior structures of the planets of the solar system indicates that MgO is likely found in solid state and in the B2 phase within all these objects due the steep increase of the melting temperature with increasing pressure.

ACKNOWLEDGMENTS

Part of this work was supported by the ANR Grant No. PLANETLAB 12-BS04-0015. Funding and support from Paris Sciences et Lettres (PSL) university through the project origins and conditions for the emergence of life is also acknowledged. This work was performed using HPC resources from GENCI- TGCC (Grant No. 2017-A0030406113) and was granted access to the HPC resources of MesoPSL financed by the Region Ile de France and the project Equip@Meso (Reference No. ANR-10-EQPX-29-01) of the programme Investissements d'Avenir supervised by the Agence Nationale pour la Recherche

[1] T. Duffy, N. Madhusudhan, and K. K. M. Lee, *Treatise on Geophysics*, 2nd ed. (Elsevier, Amsterdam, 2015), Vol. 2, p. 149.
[2] D. Alfè, Phys. Rev. Lett. **94**, 235701 (2005).
[3] A. B. Belonoshko, S. Arapan, R. Martonak, and A. Rosengren, Phys. Rev. B **81**, 054110 (2010).
[4] D. Valencia, D. D. Sasselov, and R. J. O'Connell, Astrophys. J. **665**, 1413 (2007).
[5] D. Valencia, D. D. Sasselov, and R. J. O'Connell, Astrophys. J. **656**, 545 (2007).
[6] D. D. Sasselov, D. Valencia, and R. J. O'Connell, Phys. Scr. **T130**, 014035 (2008).
[7] R. S. McWilliams, D. K. Spaulding, J. H. Eggert, P. M. Celliers, D. G. Hicks, R. F. Smith, G. W. Collins, and R. Jeanloz, Science **338**, 1330 (2012).
[8] F. Coppari, R. F. Smith, J. H. Eggert, J. Wang, J. R. Rygg, A. Lazicki, J. A. Hawreliak, G. W. Collins, and T. S. Duffy, Nat. Geosci. **6**, 926 (2013).
[9] D. Cebulla and R. Redmer, Phys. Rev. B **89**, 134107 (2014).
[10] S. Root, L. Shulenburger, R. W. Lemke, D. H. Dolan, T. R. Mattsson, and M. P. Desjarlais, Phys. Rev. Lett. **115**, 198501 (2015).
[11] R. M. Bolis, G. Morard, T. Vinci, A. Ravasio, E. Bambrink, M. Guarguaglini, M. Koenig, R. Musella, F. Remus, J. Bouchet, N. Ozaki, K. Miyanishi, T. Sekine, Y. Sakawa, T. Sano, R. Kodama, F. Guyot, and A. Benuzzi-Mounaix, Geophys. Res. Lett. **43**, 9475 (2016).
[12] K. Miyanishi, Y. Tange, N. Ozaki, T. Kimura, T. Sano, Y. Sakawa, T. Tsuchiya, and R. Kodama, Phys. Rev. E **92**, 023103 (2015).
[13] B. Boates and S. A. Bonev, Phys. Rev. Lett. **110**, 135504 (2013).
[14] J. B. Pollack, O. Hubickyj, P. Bodenheimer, J. J. Lissauer, M. Podolak, and Y. Greenzweig, Icarus **124**, 62 (1996).
[15] X. Gonze, B. Amadon, P. M. Anglade, J. M. Beuken, F. Bottin, P. Boulanger, F. Bruneval, D. Caliste, R. Caracas, M. Côté, T. Deutsch, L. Genovese, P. Ghosez, M. Giantomassi, S. Goedecker, D. R. Hamann, P. Hermet, F. Jollet, G. Jomard, S. Leroux *et al.*, Comput. Phys. Commun. **180**, 2582 (2009).
[16] D. M. Ceperley and B. J. Alder, Phys. Rev. Lett. **45**, 566 (1980).
[17] Z. Wu, R. M. Wentzcovitch, K. Umemoto, B. Li, K. Hirose, and J.-C. Zheng, J. Geophys. Res. (Solid Earth) **113**, B06204 (2008).
[18] F. Jollet, M. Torrent, and N. Holzwarth, Comput. Phys. Commun. **185**, 1246 (2014).
[19] N. A. W. Holzwarth, A. R. Tackett, and G. E. Matthews, Comput. Phys. Commun. **135**, 329 (2001).
[20] R. M. Martins, *Electronic Structure* (Cambridge University Press, Cambridge, 2004).
[21] P. Allen M and D. J. Tidsley, *Computer Simulations of Liquids* (Oxford University Press, Oxford, 1989).
[22] R. Musella, Ph.D. thesis, University Paris Diderot, 2016.
[23] J. Bouchet, S. Mazevet, G. Morard, F. Guyot, and R. Musella, Phys. Rev. B **87**, 094102 (2013).
[24] W. B. Holzapfel, M. Hartwig, and W. Sievers, J. Phys. Chem. Ref. Data **30**, 515 (2001).
[25] L. V. Al'Tshuler, S. E. Brusnikin, and E. A. Kuz'menkov, J. Appl. Mech. Tech. Phys. **28**, 129 (1987).
[26] A. B. Belonoshko, P. I. Dorogokupets, B. Johansson, S. K. Saxena, and L. Koči, Phys. Rev. B **78**, 104107 (2008).

[27] J. Bouchet, F. Bottin, G. Jomard, and G. Zérah, Phys. Rev. B **80**, 094102 (2009).
[28] J. D. Kubicki and A. C. Lasaga, Am. J. Sci. **292**, 153 (1992).
[29] A. B. Belonoshko, Geochim. Cosmochim. Acta **58**, 4039 (1994).
[30] A. J. C. Ladd and L. V. Woodcock, Mol. Phys. **36**, 611 (1978).
[31] A. B. Belonoshko, N. V. Skorodumova, A. Rosengren, and B. Johansson, Phys. Rev. B **73**, 012201 (2006).
[32] T. Taniuchi and T. Tsuchiya, J. Phys.: Condens. Matter **30**, 114003 (2018).
[33] J. P. Poirier, *Introduction to the Physics of the Earth's Interior* (Cambridge University Press, Cambridge, 2004).
[34] S. Mazevet, M. Torrent, V. Recoules, and F. Jollet, High Energy Density Phys. **6**, 84 (2010).
[35] T. Guillot and D. Gautier, *Treatise on Geophysics*, 2nd ed. (Elsevier, Amsterdam, 2015), Vol. 10, p. 529.
[36] K. Umemoto, R. M. Wentzcovitch, and P. B. Allen, Science **311**, 983 (2006).
[37] Y. Miguel, T. Guillot, and L. Fayon, Astron. Astrophys. J. **596**, A114 (2016).
[38] B. Militzer, Phys. Rev. B **87**, 014202 (2013).
[39] N. Nettelmann, A. Becker, B. Holst, and R. Redmer, Astrophys. J. **750**, 52 (2012).
[40] G. Morard, J. Bouchet, D. Valencia, S. Mazevet, and F. Guyot, High Energy Density Phys. **7**, 141 (2011).